PHYSICAL REVIEW C **95**, 034612 (2017)

Performance of the Fourier shape parametrization for the fission process

C. Schmitt,[1,*] K. Pomorski,[2] B. Nerlo-Pomorska,[2] and J. Bartel[3]

[1]*Grand Accélérateur National d'Ions Lourds, CEA/DSM-CNRS/IN2P3, F-14076 Caen, France*

[2]*Uniwersytet Marii Curie Skłodowskiej, Katedra Fizyki Teoretycznej, PL-20031 Lublin, Poland*

[3]*IPHC, Université de Strasbourg-CNRS, F-67037 Strasbourg, France*

(Received 6 December 2016; published 22 March 2017)

The availability of realistic potential energy landscapes in restricted deformation space is the prerequisite starting point for modeling several nuclear properties and reactions, namely large-amplitude phenomena. The achievement of a macroscopic-microscopic approach, employing an innovative four-dimensional (4D) nuclear shape parametrization based on a Fourier expansion, and a realistic potential-energy prescription, is presented. A systematic analysis of the 4D deformation energy landscapes over an extended region of the nuclear chart from Pt to Pu is performed, searching for fission valleys, as well as exotic ground and metastable states. The significance of the approach for predicting mass partitioning in low-energy fission is demonstrated. The ability of the model to address shape-driven effects, like stable octupole and very elongated isomeric configurations, is discussed, too. The proposed approach constitutes an efficient framework for an extended model of fission dynamics over a wide range of fissioning mass, excitation energy, and angular momentum.

DOI: 10.1103/PhysRevC.95.034612

I. INTRODUCTION

Nuclear fission involves the decay of an initially compact compound system into two distinct fragments. The intricate re-arrangement of the nucleons which occurs along the evolution of the shape from the mononuclear to the di-nuclear configuration represents a process difficult to model. At the same time, it is a rich laboratory for learning about fundamental nuclear properties [1]. In spite of the impressive theoretical progress made in recent years, guided by increasingly innovative experiments, a unified theoretical framework for fission has not emerged yet. Powerful models do yet exist. Their validity is, in a vast majority of cases, limited to a specific range in either fissioning mass, excitation energy, or angular momentum. This range depends on the specific assumptions used to make the calculation tractable. Indeed, accounting simultaneously and in detail for all features entering into play when a nucleus goes to fission is extremely challenging, and computation-wise prohibitive. It is the goal of this work to make a step into the direction of the development of an efficient, as realistic as possible, unified model of fission, in particular, and large-amplitude phenomena, in general.

To address the physics of fission, three main ingredients are required: a parametrization of the nuclear shape, a prescription for the energy of the nucleus as a function of its deformation, and the equations governing its evolution with time. The validity range of the model is determined by the specific choices made for these ingredients. As an obvious example, we mention the account of quantum effects in the potential energy calculation: While it is justified to neglect these for describing fission at high excitation energy, they are indispensable for understanding low-energy fission. This paper focuses on the first two ingredients entering the theoretical description of fission, first introduced in Ref. [2]. An innovative model is presented, employing (i) a particularly flexible 4D shape parametrization, and (ii) an accurate prescription for the calculation of the potential energy within the macroscopic-microscopic approach. Although of purely static nature, deformation energy landscapes are the necessary starting point for modeling many nuclear properties and reactions. The quality of the landscape has a direct impact on the predictive power of any model based on it [3]. The achievement of the present model is studied in detail in this work, and confronted wherever possible, to experimental observations, over an extended region of the nuclear chart. Its potentiality for describing large-amplitude phenomena, and its subsequent extension to the modeling of fission dynamics is discussed.

In Sec. II the theoretical framework is presented with special emphasis on the innovative shape parametrization, probing its convergence and deriving optimal collective coordinates. The macroscopic-microscopic method employed to calculate the potential energy is then outlined. Results are reported in Sec. III. The properties of the identified fission valleys, and their evolution with neutron and proton numbers of the fissioning nucleus, are first presented. The occurrence of exotic ground-state and exotic isomeric states, corresponding to very deformed configurations, are next examined in detail. A comparison with experiment or predictions by other models is used to assess the relevance and accuracy of the proposed framework. Summary and conclusions are drawn in Secs. IV and V. Preliminary results of the present study have been reported in Refs. [4–6].

II. THEORETICAL FRAMEWORK

A. The Fourier shape parametrization

A precise description of nuclear shapes involving as few variables as possible is a demanding task, in particular in connection with fission. Several powerful shape parametrizations have been developed [7]. We employ here a recently proposed parametrization which allows one to cover a rich variety of shapes with four collective deformation parameters only. This

*schmitt@ganil.fr

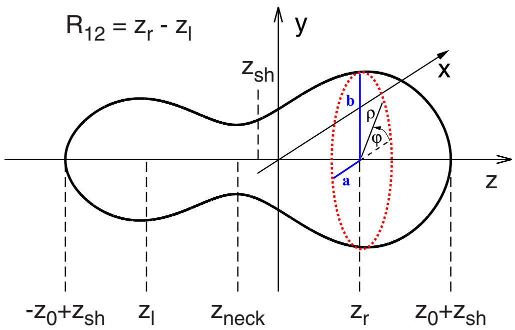

FIG. 1. Schematic visualization in cylindrical coordinates of the parameters entering the definition of the profile function defined with Eqs. (1)–(4). The quantities z_l and z_r localize the mass centers of left and right nascent fragment entering the definition of $R_{12} = z_r - z_l$.

parametrization is able to overcome some of the limitations encountered with previous prescriptions [2]; it is very rapidly converging and easy to handle, as will be demonstrated below.

1. Description

The profile function of the nuclear shape is expanded, in cylindrical coordinates, in a Fourier series [2]:

$$\frac{\rho_s^2(z)}{R_0^2} = \sum_{n=1}^{\infty} \left[a_{2n} \cos\left(\frac{(2n-1)\pi}{2} \frac{z - z_{sh}}{z_0} \right) + a_{2n+1} \sin\left(\frac{2n\pi}{2} \frac{z - z_{sh}}{z_0} \right) \right], \tag{1}$$

where $\rho_s^2(z)$ is the distance from a surface point at coordinate z to the symmetry axis (z axis in Fig. 1) and R_0 is the radius of the corresponding spherical shape having the same volume. The extension of the shape along the symmetry axis is $2z_0$ with left and right ends located at $z_{\min} = z_{sh} - z_0$ and $z_{\max} = z_{sh} + z_0$, where $\rho_s^2(z)$ vanishes, a condition which is automatically satisfied by Eq. (1). The length of the nucleus is given by $2z_0 = 2cR_0$, and can be obtained from volume conservation:

$$\frac{\pi}{3c} = \sum_{n=1}^{\infty} (-1)^{n-1} \frac{a_{2n}}{2n-1}. \tag{2}$$

Let us note that the above relation establishes a fast connection of the Fourier and the famous Funny-Hills parametrization [9], where c is the elongation parameter, that is equal to unity for the sphere, smaller (larger) than 1 for oblate (prolate) deformations.

The shift coordinate z_{sh} is chosen such that the center of mass of the nuclear shape is located at the origin of the coordinate system. The parameters a_2, a_3, a_4 describe, respectively, quadrupole, octupole, and hexadecapole deformations, which in the context of fission, are related to elongation, left-right asymmetry, and neck thickness, respectively.

To describe nonaxial shapes, the profile function, Eq. (1), is factorized [8]:

$$\varrho_s^2(z,\varphi) = \rho_s^2(z) \frac{1-\eta^2}{1+\eta^2+2\eta\cos(2\varphi)}, \tag{3}$$

TABLE I. Values of Fourier expansion coefficients for a spherical shape. Odd coefficients are zero.

$2n$	2	4	6	8	10
$a_{2n}^{(0)}$	1.03205	−0.03822	0.00826	−0.00301	0.00142

where φ is defined as usual in cylindrical coordinates (see Fig. 1). The nonaxiality parameter η is the relative difference of the half axis of the cross section perpendicular to the symmetry axis, assumed to be of ellipsoidal form,

$$\eta = \frac{b-a}{b+a}, \tag{4}$$

where the condition $ab = \rho_s^2$ ensures volume conservation for the nonaxially deformed nucleus. This definition, together with the expressions for the semiaxis,

$$a(z) = \rho_s(z)\sqrt{\frac{1-\eta}{1+\eta}} \quad \text{and} \quad b(z) = \rho_s(z)\sqrt{\frac{1+\eta}{1-\eta}}, \tag{5}$$

shows that η is independent of z. This prescription can be generalized to a z-dependent η, and nonellipsoidal cross sections, what may lead to energetically more favored configurations when approaching scission. Such an extension is beyond the scope of the present study and will be the subject of a future investigation.

The different quantities entering Eqs. (1)–(4) can be visualized in Fig. 1. There, the distance R_{12} between the centers of mass of the left and right nascent fragments is also shown, because this quantity is quite convenient and popular for fission studies. It reads

$$R_{12} = \frac{\pi \int_{z_{\text{neck}}}^{z_{\max}} \rho_s^2(z)\, z\, dz}{\pi \int_{z_{\text{neck}}}^{z_{\max}} \rho_s^2(z)\, dz} - \frac{\pi \int_{z_{\min}}^{z_{\text{neck}}} \rho_s^2(z)\, z\, dz}{\pi \int_{z_{\min}}^{z_{\text{neck}}} \rho_s^2(z)\, dz}, \tag{6}$$

where z_{neck} determines the location of the plane which separates the two nascent fragments, corresponding usually to a minimum of $\rho_s(z)$. For more compact shapes which feature no neck, the value of z_{neck} can be determined with a suitable procedure that will be explained in Appendix 4. In the Fourier parametrization, the distance R_{12} can be calculated analytically, and, for left-right symmetric shapes, is given by

$$R_{12} = 2\, R_0\, c \left[1 - \frac{6}{\pi^2} c \sum_{n=1} \frac{a_{2n}}{(2n-1)^2} \right]. \tag{7}$$

Additional quantities useful for nuclear reaction and structure studies are derived in the Appendix.

2. Convergence

An advantage of the Fourier parametrization, Eq. (1), is that it can be carried to any desired order, i.e., to any precision, and therefore its convergence can be studied. The latter is illustrated for the spherical shape in Table I, where the values of the first a_{2n} coefficients are given (the a_{2n+1} for left-right symmetric shapes are zero). Hereafter, the coefficients for the spherical shape will be referred to as $a_{2n}^{(0)}$. The Fourier series is seen to converge extremely rapidly, with, e.g., the parameter

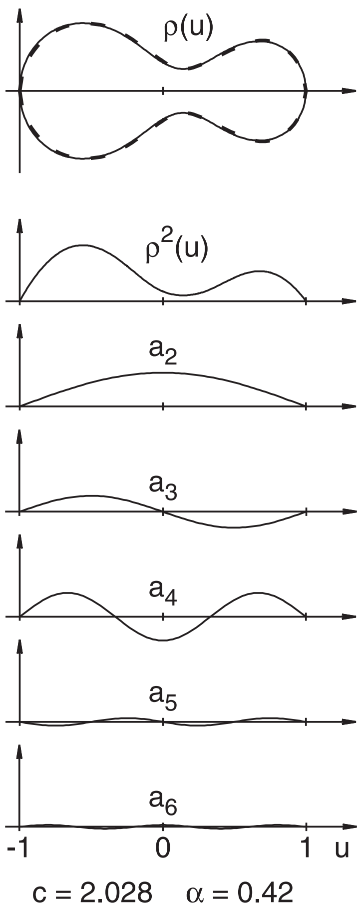

FIG. 2. Relative importance of the contributions to the shape function $\rho_s^2(z)$, Eq. (1), from different orders a_n of the Fourier series, for the left-right asymmetric shape given in the top part of the picture. Profiles are plotted as a function of the reduced variable $u = (z - z_{sh})/z_0$. The shape of the nucleus obtained within the Strutinsky optimal shapes theory [13] is shown as well with the thick dashed line.

$a_6^{(0)}$ being down by more than two orders of magnitude with respect to the leading-order parameter $a_2^{(0)}$.

For well-deformed, necked-in shapes, the convergence is illustrated in Fig. 2. The contributions from the different orders of the expansion are plotted separately, for a left-right asymmetric shape. It is seen that the lowest order a_2 coefficient determines essentially the elongation, and the next one, a_4, the neck formation. The additional inclusion of a_3 creates a left-right asymmetry, on the top of which inclusion of the next a_5 parameter generates only some minor distortions. The change in shape introduced by higher orders (even or odd) is generally small, if not negligible.

To assess the precision of the Fourier parametrization with a limited number of coefficients, we consider the liquid drop (LD) saddle-point configurations obtained with the three-quadratic-surface parametrization [3,10,11] which involves five shape degrees of freedom. These saddle-point shapes are displayed in Fig. 3 for fissility ($x = Z^2/49A$) values typical of light ^{40}Ca ($x \approx 0.2$) up to very heavy ^{278}Ds ($x \approx 0.9$) nuclei with black full contours. For each fissility, the shape profile

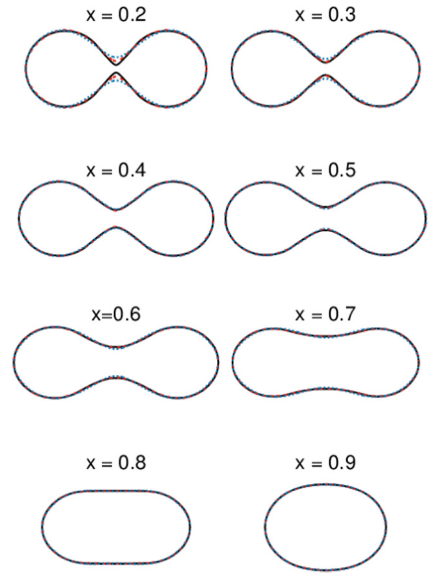

FIG. 3. Comparison of liquid drop three-quadratic saddle-point shapes (black full contours) for different values of the nuclear fissility x, and shapes generated through the Fourier series, Eq. (1), limited to a_4 (blue dotted) or a_6 (red dashed).

that can be generated by the expansion in the Fourier series, Eq. (1), is also shown when terms up to a_4 (blue dotted lines) and a_6 (red dashed lines) are included. It is observed that, in all cases, already the expansion limited to a_4 provides a very faithful description of the three-quadratic saddle-point shapes. Additional shapes generated with the three-quadratic parametrization, including left-right asymmetric ones typical of the local potential-energy extrema generated by shell effects [12], are found to be reproduced well, too, by the Fourier expansion limited to order $n = 6$. A similarly good agreement is obtained when the Fourier shapes are compared to the so-called optimal Strutinsky shapes [13], as what can be seen in Fig. 2.

One of the essential benefits of the Fourier expansion is its fast convergence. This is further demonstrated in Fig. 4, where the Lublin-Strasbourg-drop (LSD) deformation energy (see Sec. II B) is shown for ^{232}Th as a function of the elongation variable R_{12} in units of R_0. Here and throughout this work

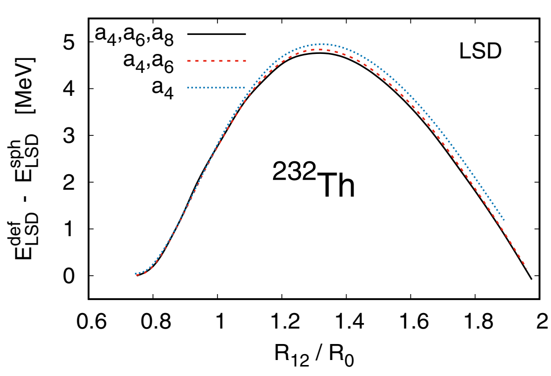

FIG. 4. LSD deformation energy relative to the spherical ground state as a function of R_{12}/R_0 for ^{232}Th with the Fourier series limited up to a_4 (blue dotted), a_6 (red dashed), and a_8 (black full line).

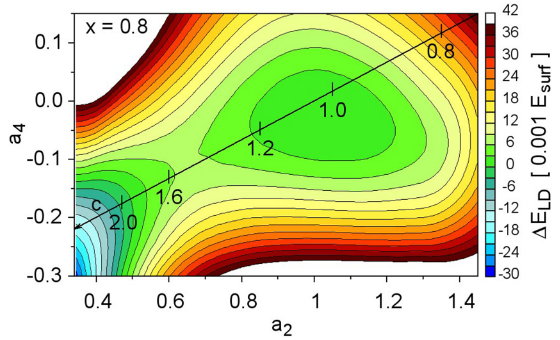

FIG. 5. LSD potential energy relative to the spherical ground state, in units of the surface energy in the (a_2, a_4) deformation plane for a nucleus with fissility x=0.8. The LSD fission path runs from the top right to the bottom left end. Corresponding values of the Funny-Hills elongation variable c [9] are indicated along the path.

potential energies are given relative to the spherical LSD minimum. The height of the macroscopic fission barrier B_f^{LSD} is seen to be decreased by about 100 keV when a_6 is included in addition to a_2 and a_4. Inclusion of higher-order terms decreases B_f^{LSD} further by a few tens of keV at most.

3. Collective coordinates

In spite of their connection to fissioning shapes, the meaning of the Fourier coefficients a_n remains limited as far as physics intuition is concerned. For example, when the nucleus gets more elongated along a typical path to fission, the value of a_2 is decreasing instead of increasing. This is illustrated in Fig. 5 for a nucleus with fissility $x = 0.8$ (e.g., ^{216}U), where the LSD potential energy, relative to the spherical ground state and given in units of the surface energy, is shown in the (a_2, a_4) plane (all other coefficients are set to zero for simplicity). As a guidance, the value of the Funny-Hills elongation parameter c [9] is indicated along the fission path. Rather than discussing fission in the space of the original Fourier coefficients a_n, we propose thus to define new "collective" coordinates q_n as linear combinations of the a_n and analyze the fission process in the space of these new coordinates. We shall demonstrate that this will allow for an optimal and efficient presentation of the potential energy in the deformation space most relevant for large-amplitude phenomena, and in particular for fission.

According to the convergence properties discussed above, only the first six orders were retained here as a starting point, and the following optimal collective deformation coordinates were determined as

$$\begin{aligned} q_2 &= a_2^{(0)}/a_2 - a_2/a_2^{(0)}, \quad q_3 = a_3, \\ q_4 &= a_4 + \sqrt{\left((q_2/9)^2 + \left(a_4^{(0)}\right)^2\right)}, \\ q_5 &= a_5 - (q_2 - 2)a_3/10, \\ q_6 &= a_6 - \sqrt{\left((q_2/100)^2 + \left(a_6^{(0)}\right)^2\right)}, \end{aligned} \tag{8}$$

where the $a_n^{(0)}$ are the values of the Fourier coefficients for the spherical shape, as given in Table I. The resulting LSD deformation energies are shown in Fig. 6 in various (q_i, q_j) subspaces for a nucleus with fissility $x = 0.8$. They exhibit a pattern which is ideally suited for modeling fission trajectories.

The above study shows that the higher-order coordinates q_5 and q_6 are, indeed, very small all along the path to fission, and that within the accuracy of the present approach, they can be set to zero. This approximation permits to parametrize analytically the higher-order Fourier coefficients as functions of the lower-order ones, with

$$\begin{aligned} a_5 &= (q_2 - 2)\,\frac{a_3}{10}, \\ a_6 &= \sqrt{\left(\frac{q_2}{100}\right)^2 + \left(a_6^{(0)}\right)^2}. \end{aligned} \tag{9}$$

All things put together, we are then able to work within a nuclear deformation space of only four dimensions with collective coordinates (η, q_2, q_3, q_4) related in a direct way to nonaxiality, elongation, left-right asymmetry, and neck thickness, respectively. For each combination of these four collective variables, the coefficients a_2, a_3, and a_4 are determined by solving the first three expressions of Eq. (8); the coefficients a_5 and a_6 are then calculated from Eq. (9), and the shape profile is finally determined through Eq. (1). Unless otherwise specified, the results presented here were obtained on the following grid:

$$\begin{aligned} &\eta \in [0, 0.21] \quad \text{with} \quad \Delta\eta = 0.03, \\ &q_2 \in [-0.5, 2.5] \quad \text{with} \quad \Delta q_2 = 0.05, \\ &q_3 \in [0, 0.21] \quad \text{with} \quad \Delta q_3 = 0.03, \\ &q_4 \in [-0.25, 0.25] \quad \text{with} \quad \Delta q_4 = 0.05. \end{aligned}$$

Within this "*hypercube*," the potential energy is calculated in a total of 42 944 points, among which only a few at largest deformations $q_2 \geqslant 2$ have to be excluded from the analysis as they do not correspond to compact (mononuclear) shapes. The number of points is increased for specific investigations, whenever a more dense mesh is required. The parametrization is easily expendable to higher orders, by means of the introduction of additional Fourier coefficients a_n. This has no impact on the definition of the collective coordinates which remain at the number four. It simply makes their numerical value more and more precise. We emphasize that the parametrization is an expansion in terms of a_n, which constitutes a basis of independent deformation parameters. Convergence is to be discussed in terms of these coefficients, and not in terms of the q_i's.

B. Potential energy

The potential energy of the system is calculated within the macroscopic-microscopic approach. The total energy $E_{\mathrm{tot}}(\eta, q_2, q_3, q_4)$ of a nucleus with a given deformation is calculated as

$$E_{\mathrm{tot}} = E_{\mathrm{mac}} + E_{\mathrm{mic}}, \tag{10}$$

where each contribution depends, although not explicitly specified, on deformation. The macroscopic part $E_{\mathrm{mac}} = E_{\mathrm{LSD}}$ is calculated within the LSD model [14] which is a liquid-drop-type parametrization of the nuclear energy including

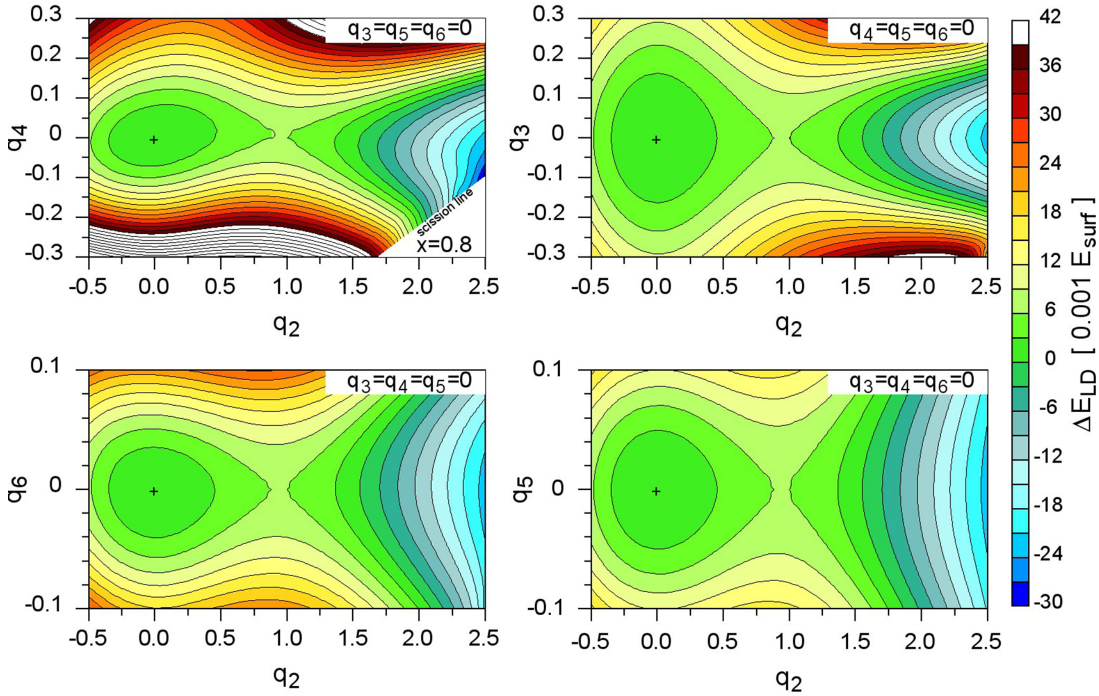

FIG. 6. LSD potential energy in the (q_2, q_4) (top left), (q_2, q_3) (top right), (q_2, q_6) (bottom left), and (q_2, q_5) (bottom right) deformation subspaces for a nucleus with fissility x=0.8. In each (q_i, q_j) plot, the collective coordinates q_k with $k \neq i, j$ are set to zero.

a curvature $A^{1/3}$ term in the leptodermous expansion and a deformation-dependent congruence energy term [15]. The LSD prescription has shown to yield a good description of both nuclear ground-state masses and fission-barrier heights. The microscopic part consists of the proton and neutron shell and pairing corrections [16–18]:

$$E_{\rm mic} = E_{\rm shell} + E_{\rm pair}. \tag{11}$$

For each kind of particle, shell corrections are obtained by subtracting the average energy from the sum of the single-particle (s.p.) energies:

$$\mathrm{E}_{\rm shell} = \sum_k e_k - \widetilde{E}. \tag{12}$$

The smooth energy $\widetilde{E}$ is evaluated using the Strutinsky prescription [17,18]. Pairing corrections are obtained as the difference between the BCS [16] energy and the s.p. energy sum, minus the average pairing energy [16,19].

$$E_{\rm pair} = E_{\rm BCS} - \sum_k e_k - \langle E_{\rm pair}\rangle. \tag{13}$$

The s.p. wave functions and s.p. energies e_k are obtained as the eigenstates and eigenvalues of the Yukawa-folded mean-field potential [20,21] at given (η, q_2, q_3, q_4) deformation. An approximate particle-number projection was included when solving the BCS equations [22].

The potential energy with its macroscopic and microscopic contributions is calculated on each mesh point of the aforementioned grid. Unless explicitly specified, and to limit computing time, the proton and neutron s.p. levels were calculated exactly for a number of "seed" nuclei, only, and suitably scaled [17], for calculating those of the neighboring nuclei with N and Z up to $N_{\rm seed} \pm 2$ and $Z_{\rm seed} \pm 2$, where $N_{\rm seed}$ and $Z_{\rm seed}$ are the neutron and proton number of the seed nucleus, respectively. This scaling was checked to give results that differ from the exact solution by a few hundreds of keV at most.

The macroscopic-microscopic approach outlined above, but used with different shape parametrizations, has shown successful in understanding the gross evolution of fission properties over a large domain by our collaboration [17,23,24]. The relevance of the calculation of the microscopic energy was recently demonstrated in an independent work [25] focusing on the detailed description of fission modes in Th and U nuclei. Further improvement can be envisaged, with the implementation of the alternative Strutinsky method of Ref. [26] and by using a surface-dependent pairing, rather than a constant pairing strength [27]. This is beyond the scope of the present investigation.

III. RESULTS

Calculations along isotopic and isotonic chains of around 100 even-even nuclei between Pt ($Z = 78$) and Pu ($Z = 94$) have been performed with the macroscopic-microscopic model presented in Sec. II. The topography of the 4D landscapes was analyzed in detail. Depending on the specific phenomenon under study, minimization with respect to one or the other coordinate was carried out. Extrema (absolute and local minima, as well as saddles), ridges, and valleys were searched for. Because the main interest of the present paper is on fission, the presentation of the results starts with fission properties, before discussing exotic stable and metastable configurations.

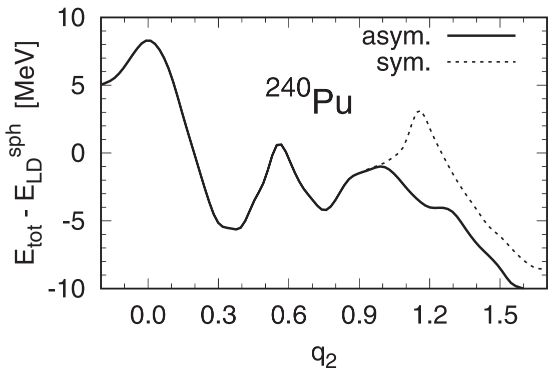

FIG. 7. Macroscopic-microscopic potential energy as a function of q_2 for the nucleus ^{240}Pu after minimization with respect to the other deformation parameters. The lowest-energy left-right asymmetric path (solid line) as well as the path imposing left-right symmetry (dashed line) are shown.

A. Fission barriers

A careful research of absolute and local extrema was carried out using the approximation procedure of Ref. [28], yielding the location of the stable ground state, possible metastable fission isomeric states, as well as the saddles separating them. Different specific paths to fission (e.g., left-right symmetric or asymmetric) can be investigated, as a function of different collective coordinates, applying a suitable minimization procedure with respect to the remaining coordinates. The resulting 1D potential energy is shown in Fig. 7 as a function of the elongation parameter q_2 for the nucleus ^{240}Pu along the energetically most favorable asymmetric path with the solid line, while the symmetric path is given by the dashed line. One observes the well-known features in this mass region: namely, a double-humped barrier with a left-right symmetric first saddle, and a second saddle which is left-right asymmetric. The magnitude of the effect depends on the specific nucleus under consideration, as it is widely connected to the microscopic contribution to the potential energy. A critical influence of nonaxiality was observed in our work in the vicinity of the ground state, only. Several models have predicted a nonaxial first saddle point (see, e.g., Ref. [29]). The present model does, however, not exhibit such an instability with respect to η. Within the accuracy of the present calculation, we estimate the influence of nonaxiality in lowering the first barrier up to a few 100 keV at most, for elements up to Pu, in accordance with Ref. [30]. The fact that other studies found a larger influence was recently connected [31] to the specificities of the "traditional" β,γ [32] shape parametrization used there. We emphasize that it is only thanks to the properties of the four collective coordinates constructed for, and defining, the present shape parametrization that this limitation of the β,γ parametrization could be revealed. We emphasize again the fact that the four coordinates are of equal importance for our analysis, and that it is only after a careful inspection of their respective contribution to a specific property that a given collective variable (i.e., nonaxiality, here) can possibly be neglected.

The height of inner and outer fission barriers obtained with the above presented prescription for the potential-energy calculation, but different shape parametrizations, was discussed in Refs. [30,33] and found in good agreement with the experiment. The barrier heights obtained with the Fourier parametrization agree, within the accuracy of the models (a few hundred keV), with the ones obtained in Refs. [30,33], and therefore, are not discussed here again (we refer to Table III in Ref. [30] and Fig. 2 in Ref. [33]). Barrier heights emerge from a one-dimensional representation (after minimization) which somehow hides the richness of the multidimensional deformation space. Other fission properties, in particular the path in this multidimensional landscape, depend more strongly on the shape parametrization. Hence, we will focus on this aspect in the next sections.

B. Fission valleys

We identify as a fission valley a continuous path, or "tunnel," running through the 4D space, with the criterion of slowly varying values along each coordinate. The same applies for the identification of the ridge separating two valleys, which can be seen as a sequence of neighboring saddles.

Since the early times of fission discovery, experiments established that low-energy fission is strongly asymmetric in the heavy U ($Z = 92$) region. It fast became an admitted fact that this asymmetry originates from the influence of shell effects in the nascent fragments. With increasing atomic and mass numbers, symmetric fission is somewhat abruptly recovered for the nucleus ^{258}Fm ($Z = 100$). Here, again, it was interpreted as being caused by shell effects, namely the proximity of an energetically favored partitioning into two closed-shell ^{132}Sn fragments. For elements lighter than U, a progressive transition from asymmetric to symmetric splitting was established by the seminal experiment of Schmidt *et al.* [34]. The transition was found located around ^{226}Th ($Z = 90$). Schematically, heavier nuclei fission predominantly asymmetrically, while lighter systems fission symmetrically. In this context, the recent experimental observation of Andreyev *et al.* [35] of asymmetric low-energy fission of ^{180}Hg ($Z = 80$) came as a surprise: According to the understanding acquired with actinides, it was expected that this nucleus would preferentially split into two shell-stabilized ^{90}Zr fragments. The discovery by Andreyev *et al.* triggered intense theoretical effort, and advanced models offer different interpretations (see, e.g., Refs. [36–39]). Independently of the disagreement between different theories, the now-available data strongly suggest that an interesting evolution of driving forces in fission occurs between Hg and the trans-actinides. Unfortunately, almost no data exist on low-energy fission of elements situated midway. In parallel to the theoretical effort, tremendous experimental research activity in the region was thus initiated at various laboratories around the world (see, e.g., Refs. [40–45]).

By studying the region from Pt ($Z = 78$) to Pu ($Z = 94$), the ability of the proposed model to describe the robust evolution established in the actinides, on one side, and the striking difference exhibited by the neutron-deficient Hg, on the other side, can be probed. A comparison with the experiment permits one to benchmark the model. This is a necessary request to give credit to its predictions in the still poorly known intermediate territory. In this respect, the Po

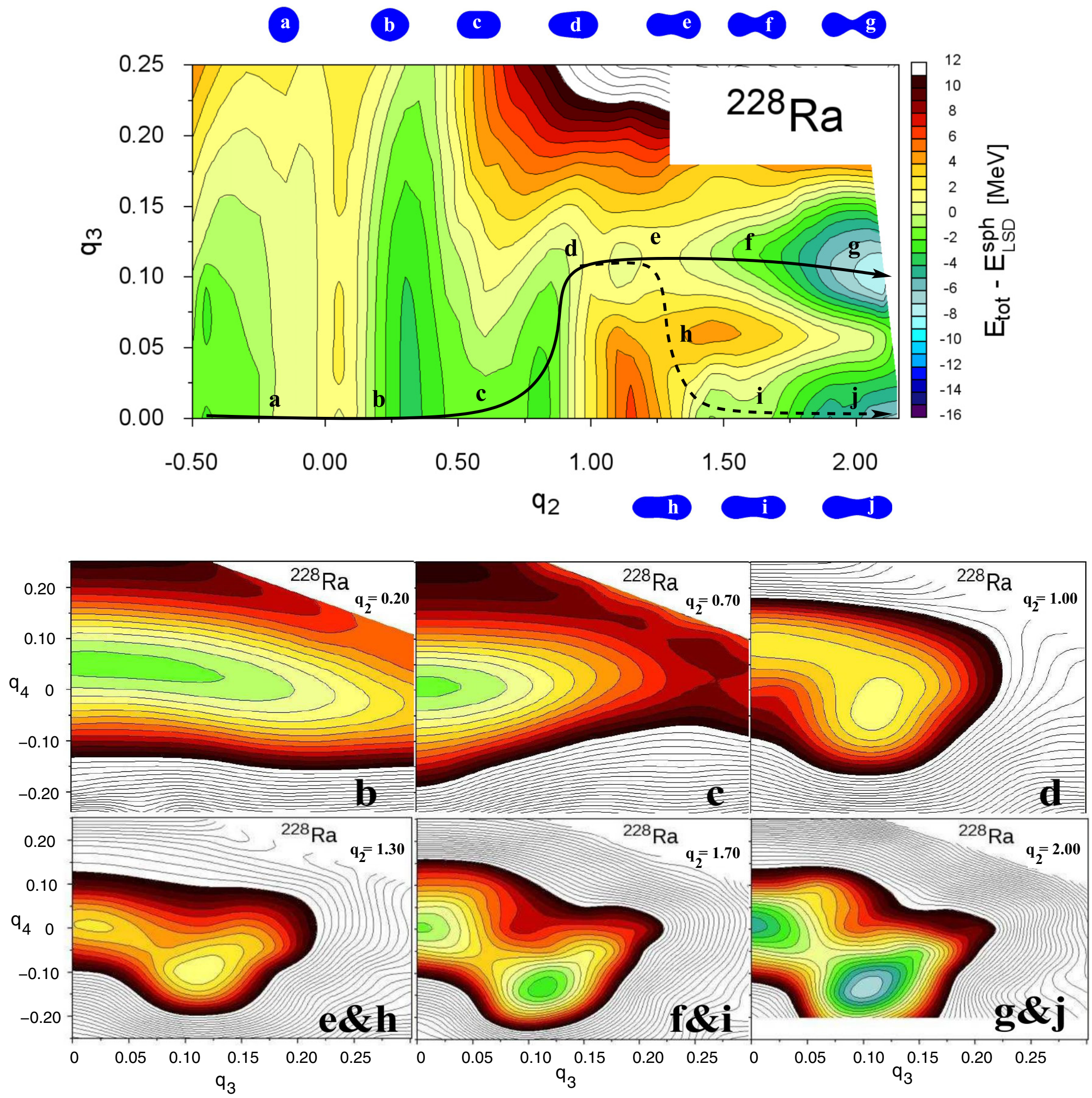

FIG. 8. (Top) Macroscopic-microscopic potential energy in the (q_2, q_3) plane for ^{228}Ra. The two identified fission paths are paved by dashed and solid curves. (Bottom) Sequence of (q_3, q_4) potential energy maps for selected values of q_2 along the fission paths identified in the top panel: $q_2 = 0.2$ (b), $q_2 = 0.7$ (c), $q_2 = 1.0$ (d), $q_2 = 1.3$ (e) and (h), $q_2 = 1.7$ (f) and (i), $q_2 = 2.0$ (g) and (j). Representative shapes along the asymmetric and symmetric paths are displayed in the top and bottom of the upper figure, respectively, and labeled with small letters along the paths (a)–(j).

$(Z = 84)$ isotopic chain constitutes a particularly relevant case, as it is ideally situated on the way between Hg and traditional actinides, and experimental data, although of very low statistics, are becoming available [40,46].

The method used to determine fission valleys is illustrated by taking ^{228}Ra as an example in Sec. III B 1. The systematic analysis, with presentation and discussion of potential energy landscapes (PEL) over the extended region, follows in Sec. III B 2. Finally, the Pu chain is discussed separately in Sec. III B 3.

1. Example of a PEL analysis: The case of ^{228}Ra

The potential energy landscape in the (q_2,q_3) plane, as obtained after minimization with respect to η and q_4, is shown in the upper part of Fig. 8 for ^{228}Ra. On top of the map, the two fission paths which we have identified, leading to symmetric (dashed line) and asymmetric fragment-splitting (solid line), are drawn. Around these two paths, the nonaxiality coordinate η was found to evolve smoothly, and to be small beyond the first barrier, as discussed in Sec. III A. Hence, nonaxiality plays no role in the emergence of two distinct paths beyond the second (isomeric state) minimum. On the contrary, the evolution of q_4 is crucial in explaining the splitting of the initially common path into two. This is demonstrated in the lower part of Fig. 8, where the potential energy, prior minimization with respect to q_4, is displayed in the (q_3, q_4) plane for specific q_2 values. It is seen that, up to $q_2 \approx 1.25$, a single minimum in the (q_3, q_4) plane exists: The shapes b, c, d correspond, respectively, to the single minimum seen in the (q_3, q_4) plane at $q_2 = 0.2$,0.7, and 1.0. Beyond the isomeric state, the path is found to

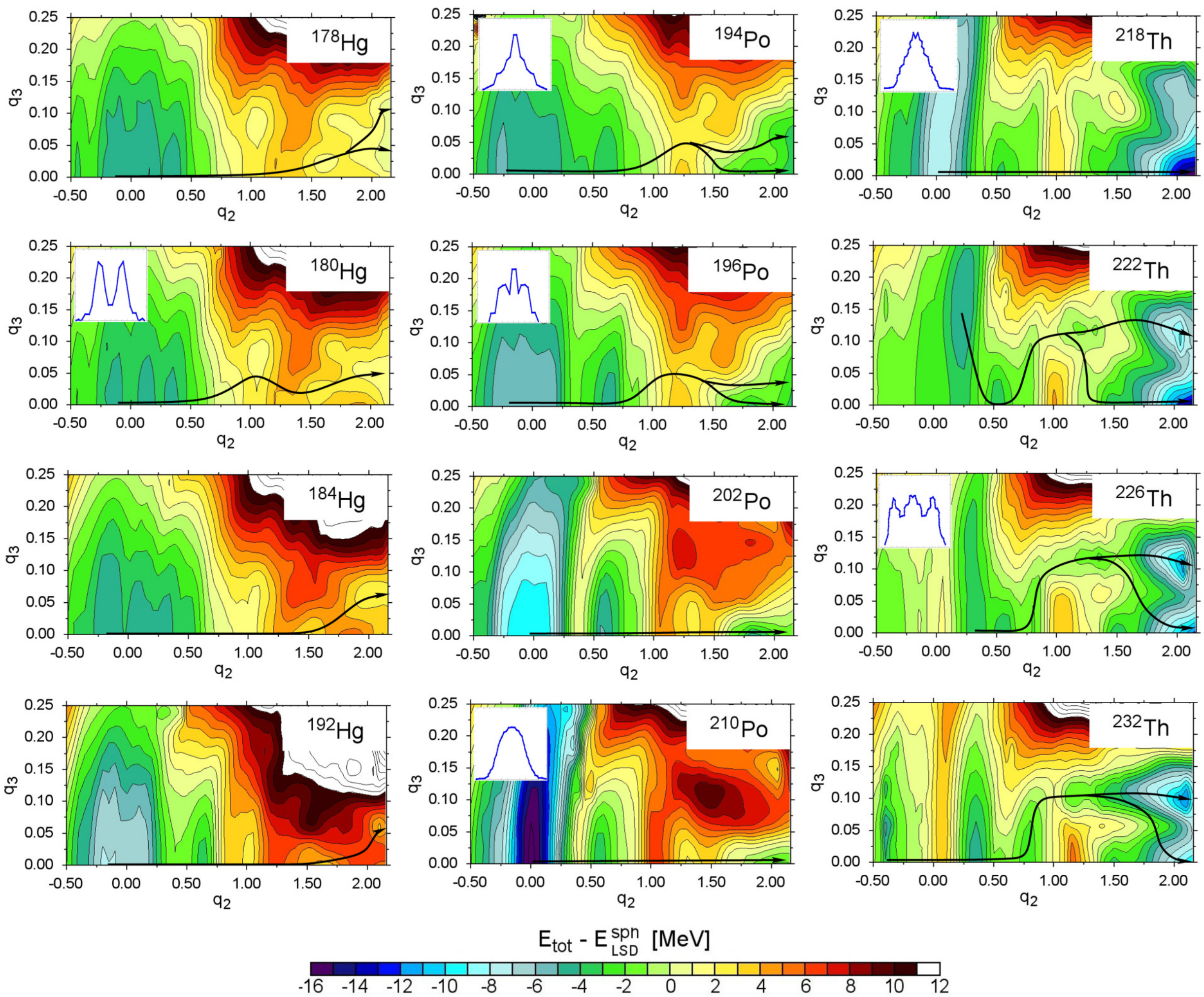

FIG. 9. Macroscopic-microscopic potential energy in the (q_2, q_3) plane for several isotopes of Hg (left column), Po (middle column), and Th (right column). The identified fission paths are indicated by a solid black line. Insets show, where available, experimental data [34,40,46,50] on fission-fragment mass or charge distribution at low excitation energy.

split because of the appearance of two separate minima in the (q_3, q_4) plane: the shapes e, f, g, and, h, i, j, refer, respectively, to these two minima along the asymmetric and symmetric paths at $q_2 = 1.3, 1.7$, and 2.0. Distinct outer saddle points for the symmetric and asymmetric channels are thus observed in this example of ^{228}Ra. The representative shapes, obtained along each path for the corresponding (q_2, q_3, q_4) combinations, show a clear difference in the profile function: The asymmetric channel is observed to be more compact than the symmetric one. The location of the asymmetric valley in the 4D deformation space corresponds to a mass partition for the nascent fragments of 94/134. This result is in good agreement with the experimental mass split [47].

The above analysis illustrates how "tunnels" related to different channels can progressively develop across the 4D deformation space, and finally lead to different exit valleys. One further notices that, at the largest elongations, it is the asymmetric valley that is lowest in energy, thus suggesting the dominance of asymmetric over symmetric fragment partition in the low excitation-energy fission of ^{228}Ra. This is in accordance with the experimental observation [47], where a triple-humped fragment-mass distribution was measured with the asymmetric contribution being most intense.

2. *Extended overview from Hg to actinides*

As mentioned earlier, a systematic analysis of the 4D landscapes was carried out for around 100 even-even nuclei between Pt and Pu. A selection of 2D (q_2, q_3) maps obtained after minimization with respect to η and q_4 are presented in Fig. 9. Isotopes of Hg, Po, and Th have been chosen because they allow one to scan the main trends in fission properties over the more extended region, and they also permit relevant confrontation with experiment in several cases. The fission paths revealed in our analysis are superimposed on the maps with thick lines.

Figure 9 shows that, depending on the isotope, either a single (symmetric or asymmetric) fission path is observed, or two distinct paths coexist. We note that, in the latter situation, the two paths separate from one another at, or slightly beyond, the outer saddle point. The maps also suggest that, while the dependence of landscape and fission path on the neutron number N of the fissioning nucleus is obvious and substantial, the dependence on the proton number Z is even stronger. This was confirmed by the systematic survey over the entire region which we have performed [6]. In the same line, when two valleys coexist, their relative depth depends more on Z than on N.

Quantitative predictions of the fission-fragment mass or charge distribution would require one to add the dynamics on top of the so-far static picture. This is beyond the scope of the present work. Nevertheless, because a realistic potential energy landscape is an indispensable ingredient in any dynamical calculation [48,49], a qualitative comparison of the 2D maps of Fig. 9 with the low-energy fission experiment is already worth the effort. The fragment mass or charge distributions as measured for several cases have thus been added to Fig. 9 as insets. It is observed that the properties of the calculated fission paths are in direct line with the profile of the experimental distribution in all these cases. One notices in particular the following:

(i) Exclusively asymmetric fission for ^{180}Hg with the identification of a single asymmetric path.
(ii) Symmetric fission for ^{218}Th with the identification of a single symmetric path.
(ii) A coexistence of asymmetric and symmetric fission for ^{226}Th with the identification of two valleys.

This consistency between our potential energy maps and the experimental data thus gives confidence into the realistic character of the proposed 4D approach, and makes promising its use in dynamical simulations.

Finally, we draw special attention to the Po isotopic chain, because it seems to exhibit a large variety of fission properties, similarly to, e.g., the Th isotopes, but in a reversed manner with increasing N value. While the mass distribution in low-energy fission of ^{210}Po was measured to be broad and predominantly symmetric [50], the low-statistics data that became available very recently [46] for the most neutron-deficient Po isotopes suggest a possible triple-humped distribution (see the corresponding insets in Fig. 9). Recall that along the Th chain, the distribution changes from symmetric to triple-humped when N is increasing (and not decreasing like for Po). The energy landscapes obtained in our theoretical approach are thus in agreement with the experimental conjecture, supporting a reversed trend along the Po and Th chains, as seen in the last second and third columns of Fig. 9. To further support this expectation we recall that for fission of ^{228}Ra as a typical actinide, we noticed in the previous section a good agreement between the mass split corresponding to the asymmetric valley and the experimental result. Extending here the comparison to the pre-actinide region, the expected most favorable mass partition for ^{180}Hg and ^{196}Po is 100/80 and 109/87, respectively, in somewhat remarkable agreement with the experimental estimate of 100/80 and 108/88 [40].

3. *The Pu chain*

An interesting evolution of the fragment mass distribution was evidenced in spontaneous fission along the Pu chain [51]. The heavy-fragment mass peak, consisting of two components centered, respectively, at $A \approx 134$ and 140, exhibits a change of the relative weight of these two components when the neutron number N is varied. Namely, the most intense of the two contributions moves from 140 to 134 when the Pu mass increases from 236 to 246. An attempt to address this observation is made in this section, by looking in detail at the structure of the asymmetric fission valley. We emphasize that, for this specific purpose, no scaling was used to compute the single-particle levels entering the calculation of E_{mic}; they were computed explicitly for every isotope. On the other hand, nonaxiality was not accounted for, as it has no influence, as we have seen before, in the vicinity and beyond the outer barrier [29], which is the range of interest here.

The potential energy landscape in the (q_2,q_3) plane, after minimization with respect to q_4, is shown in Fig. 10 for three isotopes of Pu. The asymmetric valley ($q_3 \geqslant 0.05$) clearly exhibits some structure for $1.5 \leqslant q_2 \leqslant 2$, what we connect to the existence of two asymmetric components in our model [52], one centered around 134, and the other around 142, for the heavy fragment mass. Interestingly, with increasing Pu mass, the valley gets more structured, and the 134 component starts at shorter elongation. Although we tentatively anticipate that this change in structure of the valley can yield a more intense contribution from the 134 channel for the heaviest Pu isotopes, this conjecture remains speculative and needs more advanced dynamical calculations to be verified. The difference in the shapes associated with the two asymmetric components is sketched for ^{246}Pu in the bottom right panel of Fig. 10. For an elongation coordinate fixed here at $q_2 = 2.0$, the 134 channel is characterized by a shorter, more compact shape (because of different q_3 and q_4 values), as compared to the 142 channel, in accordance with expectation.

The shape of the heavy fragment in the 134 channel is observed to be less compact than it should ideally be to prefigure a close-to-spherical nascent fragment. This shows the limitation of the proposed parametrization when approaching scission, and is because of the fact that it does not explicitly allow for independent deformations of the left and right halves. However, this limitation has only minor consequences for the present goal, because, in spite of it, two distinct asymmetric channels do emerge as expected. In addition, the fissioning configurations in the 134 and 142 channels have the expected properties, with the former being less elongated than the latter. That is, the collective coordinates selected in the present parametrization gather the main essence of the physics, and are fully suited for our goal. Going beyond requires introducing an additional coordinate, what would make dynamical calculations less tractable.

C. Stable octupole configurations

In addition to the power of the model for discussing large deformations involved in the fission process, we propose to investigate also the smaller-deformation region. We are in particular interested in the ground-state shapes in the actinide region where octupole configurations have been either evidenced in experiment, or are expected as highly probable [53]. The calculated ground-state q_3 values are displayed as a function of neutron number in Fig. 11 for the elements Ra, Th, and U. The model is found to predict a specific

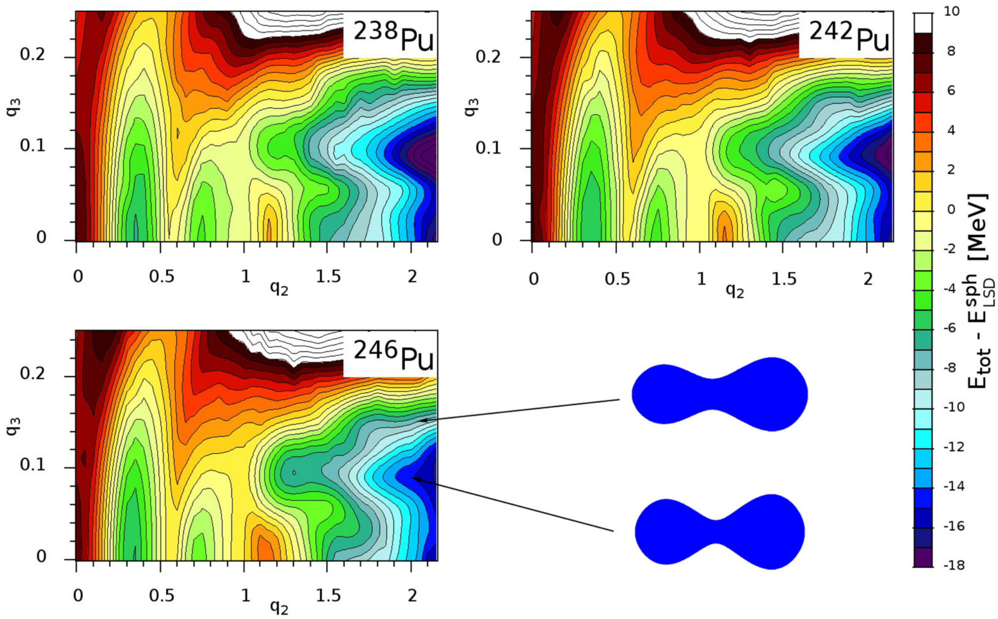

FIG. 10. Macroscopic-microscopic potential energy in the (q_2, q_3) plane for the isotopes ^{238,242,246}Pu. The shapes close to scission (q_2=2.0) in the two asymmetric channels are shown for ^{246}Pu in the bottom right panel.

window in N where static octupole deformation characterizes the ground state. This window with $N \in [130,140]$ depends to some extent on the element, and is in reasonable agreement with experiment, though, the value of N where a maximum in octupole deformation is predicted slightly differs from the experimental value $N \approx 136$. Because pairing correlations have a large influence on the energy of octupole configurations [54], the accuracy of the model may be improved on this aspect by implementing a more advanced pairing prescription.

D. Very deformed isomers and the debated existence of a third minimum

The macroscopic (LSD) fission barrier can be somewhat broad in the Pt-Pu region under consideration here. Hence, the inclusion of shell effects can produce local minima which we may identify as isomeric states. The careful survey of

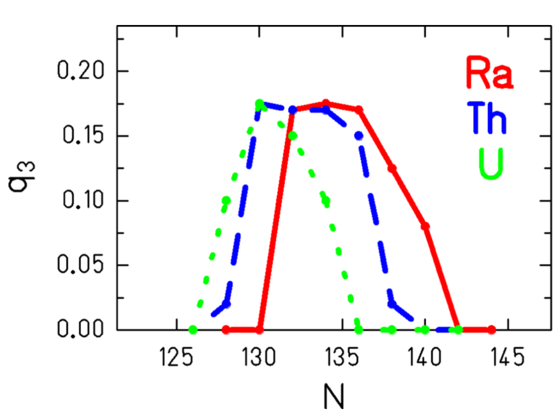

FIG. 11. Predicted octupole deformation coordinate q_3 for the ground states of Ra (red full), Th (blue dashed), and U (green dotted line) isotopes as a function of neutron number.

the 4D potential energy landscapes outlined above suggests that shell effects at large deformations can indeed yield local minima corresponding to super- and hyper-deformed shapes. A few such minima could already be guessed in the maps of Fig. 9, namely for some Po isotopes in the region $q_2 \approx 0.6$. Several strongly deformed isomers are thus predicted by the calculation. A detailed discussion of these super- and hyper-deformed states, which may trigger experimental investigation, was reported in Refs. [31,55] and is thus not repeated here.

In the present study we instead propose to address the vivid debate about the possible existence of a third minimum in the actinide region at very large deformation [56–58]. To that purpose, the evolution of the 2D potential energy landscape for four Th isotopes is presented in Fig. 12 in the (q_2,q_4) plane. Left-right asymmetry and nonaxiality have been set to zero. A shallow, 0.8 MeV (0.5 MeV when left-right asymmetry is included) deep, third minimum is observed for the lightest Th isotopes at $q_2 \approx 1.5$, but disappears with increasing neutron number. This result is in agreement with conclusions based on macroscopic-microscopic models of higher dimensionality [56,57], and self-consistent models [58], thus invalidating experimental claims (see [59] and references therein). It further illustrates the power of the present approach limited to only four dimensions, and this up to very large elongations.

IV. DISCUSSION

In this section we propose to shortly discuss the approach proposed in this work, and this as a very valuable complement to (sometimes more) elaborate models in the field.

It was demonstrated that the rich variety of possible nuclear shapes requires one to consider the following degrees of freedom: elongation, neck thickness, left-right asymmetry, and deformation of left, respectively, right, nascent fragment. That implies in principle five collective coordinates [3].

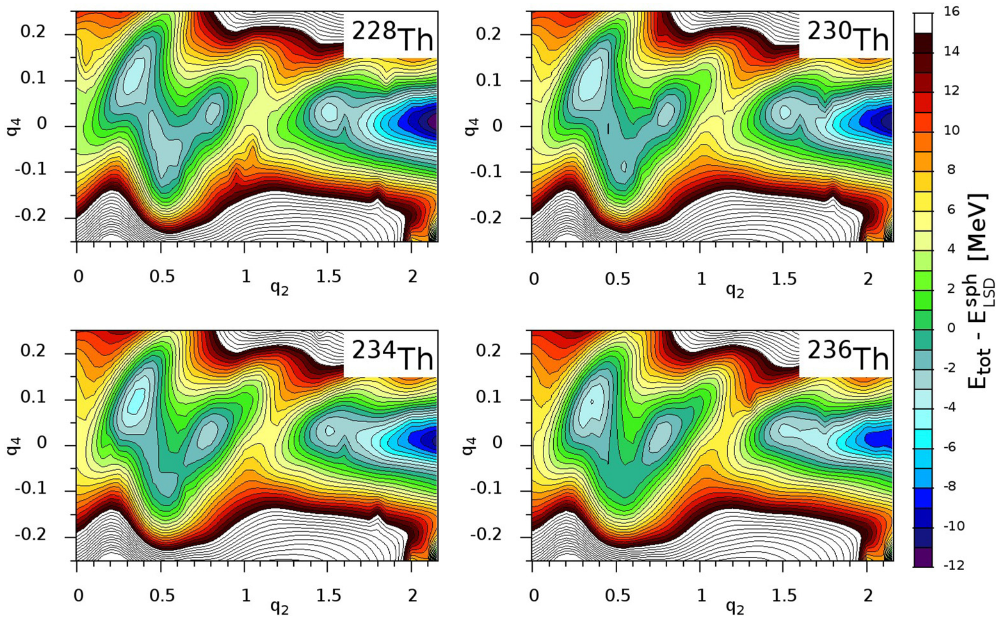

FIG. 12. Macroscopic-microscopic potential energy in the (q_2, q_4) plane for four isotopes of Th for $q_3 = 0$ and $\eta = 0$.

Unfortunately, a complete dynamical calculation in five (or more) dimensions is still difficult in practice, and models based on five shape variables, either use a simplified equation of motion [48,60], or assume as constant values some of the collective coordinates [49]. The difficulty increases with raising excitation energy, because the dynamics has to be coupled to light-particle emission [61]. Overcoming the technical and computing-time aspects remains, of course, a challenge. Yet, it is a prerequisite for the emergence of a unified framework for fission and large-scale calculations over an extended range of the nuclear chart, in excitation energy and angular momentum.

According to the results obtained in this work, the innovative Fourier parametrization of nuclear shapes, combined with LSD + Yukawa-folded macroscopic-microscopic potential energy prescription, with only four collective coordinates, turns out to be very efficient, because it explains in a reasonable manner the experimentally observed evolution of fission valleys as function of the Z and N numbers of the fissioning nucleus. Hence, the four coordinates constructed from the Fourier expansion coefficients gather the essential features of the shapes involved up to the scission configuration. This investigation has also shown its capacity to address the existence of exotic configurations.

A quantitative assessment of the performance of the approach still awaits extended dynamical calculations, which will finally determine the yield of populated fragments and their properties. Similarly, the purely static picture, which we restrict on here, requires one to be developed further to allow quantitative predictions for the probability of populating (and thus observing) exotic deformed states. The outcome of the present work constitutes a solid basis for subsequent evolution of the current (static) model.

As emphasized along the paper, the achievement of the approach relies for a large part on the assets of the Fourier parametrization. Nonetheless, we would like to stress, too, that it is really the combination of the specificities of the shape parametrization and the potential-energy prescription which determines the performance of the model. The former enables one to explore the whole variety of possible deformations for a nucleus (small-to-large), where the latter mass prescription has shown to be suited for a wide region on the nuclear chart. Hence, a unified framework is made available, using a single shape parametrization and a single potential-energy formalism over a wide range in nuclear systems and deformations. These two aspects are not always met by available models. For example, some shape parametrizations, that are very powerful around the ground state, turn out to be much less suited for fission, and *vice versa*. Similarly, some mass models are better suited in specific regions of the chart of nuclides.

The capability of the present approach of being able to cover a large spectrum of physics in a consistent way makes it, in our opinion, particularly attractive. Other elaborate models developed in the field may be more accurate for specific purposes, and/or over restricted domains. The compromise proposed here is nonetheless worth attempting, offering an efficient approach for realistic-enough predictions and tractable simulations.

V. CONCLUSIONS

Within the macroscopic-microscopic approach, an innovative efficient model is proposed to address in a unified framework various large-amplitude phenomena. The recently developed four-dimensional shape parametrization based on an expansion in terms of Fourier series is combined to the potential-energy prescription using the LSD macroscopic energy and microscopic corrections obtained from the eigenstates of a Yukawa-folded single-particle mean field.

Precise potential energy landscapes are a necessary starting point for modeling many nuclear properties and reactions in a realistic way. A detailed analysis of the 4D potential energy landscapes is thus proposed in this work and summarized for about 100 even-even isotopes between Pt and Pu. A variety of physics aspects that can be addressed through the analysis of such landscapes is illustrated to probe the accuracy of the approach. Fission paths are identified, and their evolution with Z and N is found to match experimental observations over the extended range of fissioning systems. The approach is further used to investigate the possible existence of exotic, i.e., very deformed, shape isomers, which are predicted in the Po to Th region. The presence of a very deformed third minimum in heavy actinides is also discussed, and observed to be consistent with most recent calculations.

The various investigations carried out in this work demonstrate the performance of the proposed approach. It permits one to study large-amplitude phenomena in a reasonably accurate manner, when compared with existing often much more advanced models in the field, and involving usually higher dimensionality. All this is achieved in a so-far static approach, which, however, seems to incorporate the essential physics. This achievement is mostly attributable to the specificities of the shape parametrization which converges rapidly, and to a lesser extent also to the reliability of the potential-energy formalism. The approach is going to be implemented into extended dynamics calculations, within a Langevin approach, and coupled with light-particle evaporation (see [61] and references therein).

ACKNOWLEDGMENTS

This work was partly supported by the Polish-French COPIN-IN2P3 collaboration agreement under Project No. 08-131 and by the Polish National Science Center, Grant No. 2013/11/B/ST2/04087.

APPENDIX: USEFUL PHYSICS QUANTITIES IN THE FOURIER PARAMETRIZATION

For the users more familiar with that kind of approach, several formulas for quantities commonly used in connection with nuclear reaction and structure studies are elaborated below.

1. Fourier analysis

The shape coefficients a_n can be determined, for any shape, through a Fourier analysis, taking advantage of the orthogonality relations of the trigonometric functions, leading to

$$a_{2n} = \int_{-1}^{1} \rho_s^2(u)\, \cos\left(\frac{2n-1}{2}\,\pi\, u\right) du, \tag{A1}$$

and

$$a_{2n+1} = \int_{-1}^{1} \rho_s^2(u) \sin(n\,\pi\, u)\, du, \tag{A2}$$

where u is the dimensionless variable u=(z-z_{sh})/z_0.

2. Volume conservation

Because of incompressibility of nuclear matter one assumes that the volume of a deformed nucleus is the same as for the corresponding spherical shape:

$$V = \frac{4\pi}{3} R_0^3 = \int_0^{2\pi} d\varphi \int_{z_{\min}}^{z_{\max}} dz \int_0^{\rho_s(z)} \rho\, d\rho$$
$$= \pi \int_{z_{\min}}^{z_{\max}} \rho_s^2(z)\, dz. \tag{A3}$$

This gives the following relation between the elongation parameter c [9] and all even coefficients a_{2n}:

$$\frac{\pi}{3c} = \sum_{n=1}^{\infty} (-1)^{n-1}\, \frac{a_{2n}}{2n-1}. \tag{A4}$$

This relation allows one to evaluate a_2 as a function of the elongation c and the higher order ($n > 1$) a_{2n}.

3. Fixing the center of mass

By convention the position z_{cm} of the center of mass of the deformed nucleus is set at the origin of the coordinate system; see Fig. 1. For left-right symmetric shapes this is automatically achieved by choosing the shift coordinate $z_{\rm sh} = 0$. For left-right asymmetric shapes $z_{\rm sh}$ has to be defined differently.

Imposing

$$z_{\rm cm} = \frac{\int_V z\, d^3r}{\int_V d^3r} = \frac{\pi \int_{z_{\min}}^{z_{\max}} \rho_s^2(z)\, z\, dz}{\pi \int_{z_{\min}}^{z_{\max}} \rho_s^2(z)\, dz} = 0, \tag{A5}$$

one obtains, after evaluation, the following expression:

$$z_{\rm sh} = -\frac{z_0}{2} \frac{\sum_n (-1)^{n-1}\, \frac{a_{2n+1}}{n}}{\sum_n (-1)^{n-1}\, \frac{a_{2n}}{2n-1}} = \frac{3c^2}{2\pi} R_0 \sum_n (-1)^n\, \frac{a_{2n+1}}{n}, \tag{A6}$$

where Eq. (A4) was used. For left-right symmetric shapes, $z_{\rm sh} = 0$ and the above equation implies

$$\sum_{n=1}^{\infty} \frac{a_{2n}}{n} = 0. \tag{A7}$$

4. Distance between the nascent fragments

The distance between the centers of mass of left and right fragments is given by Eq. (6). For left-right symmetric shapes, all odd coefficients a_{2n+1} vanish, and $z_{\rm neck} = 0$. Then

$$R_{12} = \frac{2\pi \int_0^{z_{\max}} \rho_s^2(z)\, z\, dz}{\frac{2\pi}{3} R_0^3}$$
$$= \frac{3}{R_0} \sum_n a_{2n} \int_0^{z_0} \cos\left(\frac{2n-1}{2}\,\pi\, \frac{z}{z_0}\right) z\, dz, \tag{A8}$$

which, after evaluation of the integrals and when using Eq. (A4), leads to Eq. (7). In the case of left-right asymmetric shapes, all the Fourier coefficients contribute and the distance between the mass centers of left and right fragments takes the more general form of Eq. (6). In this situation, we define the neck coordinate $z_{\rm neck}$ as the location where the shape $\rho_s^2(z)$ has an extremum. Such an extremum—generally a minimum in the case of a fissioning nucleus close to the scission point—always occurs, even for reasonably strong asymmetry, close to the center of the shape. One can then determine the coordinate $u_{\text{neck}} = (z_{\text{neck}} - z_{\text{sh}})/z_0$ by a Taylor expansion of the sine and cosine functions around $u = 0$. From the condition $d\rho_s^2(z)/dz = 0$ one obtains

$$u_{\text{neck}} = \frac{4}{\pi} \frac{\sum_n n\, a_{2n+1}}{\sum_n (2n-1)^2\, a_{2n}}, \tag{A9}$$

and $z_{\text{neck}} = z_{sh} + z_0\, u_{\text{neck}}$. This procedure was tested for a large variety of shapes and turns out to work very accurately as long as the shapes are not pathological.

The distance of nascent fragments R_{12} can always be written in the form,

$$R_{12} = \frac{N_R}{D_R} - \frac{N_L}{D_L}, \tag{A10}$$

with

$$N_R = \int_{z_{\text{neck}}}^{z_{\text{max}}} \rho_s^2(z)\, z\, dz \quad \text{and} \quad N_L = \int_{z_{\text{min}}}^{z_{\text{neck}}} \rho_s^2(z)\, z\, dz, \tag{A11}$$

$$D_R = \int_{z_{\text{neck}}}^{z_{\text{max}}} \rho_s^2(z)\, dz \quad \text{and} \quad D_L = \int_{z_{\text{min}}}^{z_{\text{neck}}} \rho_s^2(z)\, dz. \tag{A12}$$

In the numerators N and in the denominators D of the above expressions appear a certain number of integrals involving trigonometric functions, and one of the integration limits is the neck parameter u_{neck}. These integrals can be evaluated exactly, giving access to the most general expression for R_{12}. Specific situations are addressed below.

In the case of a left-right symmetric shape, $z_{\text{sh}} = 0$, all odd shape coefficients vanish and the quantities N_R, N_L and D_R, D_L take on the simple form,

$$N_R = -N_L = R_0^2\, z_0^2 \sum_{n=1}^{\infty} a_{2n} \left[\frac{2}{\pi} \frac{(-1)^{n-1}}{2n-1} - \left(\frac{2}{\pi} \frac{1}{2n-1} \right)^2 \right], \tag{A13}$$

and

$$D_R = D_L = R_0^2\, z_0 \sum_{n=1}^{\infty} \frac{2}{\pi} \frac{a_{2n}}{2n-1} (-1)^{n-1}, \tag{A14}$$

and consequently

$$R_{12} = 2\, z_0 \frac{\sum_n a_{2n} \left[\frac{(-1)^{n-1}}{2n-1} - \frac{2}{\pi} \frac{1}{(2n-1)^2} \right]}{\sum_n a_{2n} \frac{(-1)^{n-1}}{2n-1}}. \tag{A15}$$

In the case of a left-right asymmetric shape, according to the fast convergence of the Fourier expansion, approximate but accurate analytical expressions are already obtained when the expansion is restricted to the first leading orders a_2, a_3, and a_4. Then

$$\begin{aligned} N_R = \frac{c^2 R_0^4}{\pi} \bigg[& a_3 - \frac{3ca_3}{2} \left(\frac{2a_2}{\pi} - a_2 u_{\text{neck}} + \frac{2a_3}{\pi} \right. \\ & \left. - a_4 u_{\text{neck}} - \frac{2a_4}{3\pi} \right) + 2a_2 - \frac{4a_2}{\pi} - \pi a_2 u_{\text{neck}}^2 \\ & - \frac{2a_4}{3} - \pi a_4 u_{\text{neck}}^2 - \frac{4a_4}{9\pi} \bigg], \end{aligned}$$

$$\begin{aligned} N_L = \frac{c^2 R_0^4}{\pi} \bigg[& a_3 - \frac{3ca_3}{2} \left(\frac{2a_2}{\pi} + a_2 u_{\text{neck}} - \frac{2a_3}{\pi} \right. \\ & \left. + a_4 u_{\text{neck}} - \frac{2a_4}{3\pi} \right) - 2a_2 + \frac{4a_2}{\pi} + \pi a_2 u_{\text{neck}}^2 \\ & + \frac{2a_4}{3} + \pi a_4 u_{\text{neck}}^2 + \frac{4a_4}{9\pi} \bigg], \end{aligned}$$

$$D_R = \frac{2cR_0^3}{\pi} \left[a_2 - \frac{\pi a_2 u_{\text{neck}}}{2} + a_3 - \frac{\pi a_4 u_{\text{neck}}}{2} - \frac{a_4}{3} \right],$$

$$D_L = \frac{2cR_0^3}{\pi} \left[a_2 + \frac{\pi a_2 u_{\text{neck}}}{2} - a_3 + \frac{\pi a_4 u_{\text{neck}}}{2} - \frac{a_4}{3} \right].$$

For the dimensionless neck coordinate u_{neck} and the shift coordinate z_{sh} that enter the integrals, one obtains

$$u_{\text{neck}} = \frac{4}{\pi} \frac{a_3}{a_2 + 9a_4}, \tag{A16}$$

and

$$z_{\text{sh}} = -\frac{3c^2}{2\pi} R_0 a_3, \tag{A17}$$

which then allow one to give an estimate for R_{12} through Eq. (A10).

5. Fragment-mass asymmetry

In the Fourier parametrization, reflection-asymmetric shapes are controlled by the coefficients a_{2n+1}. For the description of the nuclear fission problem, it would now be very useful to have at hand a quantity that is directly connected to the asymmetry of the deformed nucleus along its path to the scission configuration. To this purpose one therefore introduces a mass-asymmetry parameter α that is defined as the mass difference between the two nascent fragments, normalized to the total mass of the fissioning system:

$$\alpha = \frac{A_R - A_L}{A}, \tag{A18}$$

where $A_L + A_R = A$. Assuming the nucleus to be incompressible and the partition into two pieces to take place through a sharp cutoff at the location of the neck coordinate z_{neck}, one obtains

$$\alpha = \frac{\pi \int_{z_{\text{neck}}}^{z_{\text{max}}} \rho_s^2(z)\, dz - \pi \int_{z_{\text{min}}}^{z_{\text{neck}}} \rho_s^2(z)\, dz}{4\pi R_0^3/3} = \frac{3}{4R_0^3} [D_R - D_L]. \tag{A19}$$

As noted above, D_R and D_L can be calculated by evaluating the required integrals. The derivation finally yields the following expression for the mass asymmetry:

$$\begin{aligned} \alpha = & -\frac{3c}{\pi} \sum_{n=1}^{\infty} \left\{ \frac{a_{2n}}{2n-1} \left[\sin\left(\frac{2n-1}{2} \pi\, u_{\text{neck}} \right) \right] \right\} \\ & - \frac{3c}{\pi} \sum_{n=1}^{\infty} \left\{ -\frac{a_{2n+1}}{2n} [\cos(n\pi\, u_{\text{neck}}) + (-1)^{n-1}] \right\}. \end{aligned} \tag{A20}$$

Note that, for left-right symmetric shapes, all a_{2n+1} vanish, u_{neck} becomes zero, yielding obviously $\alpha = 0$.

For the left-right asymmetric case, restricting the expansion to the leading orders gives the approximate expressions,

$$\alpha = -\frac{3c}{\pi}\left\{a_2 \sin\left(\frac{\pi u_{\rm neck}}{2}\right) - \frac{a_3}{2}[\cos(\pi u_{\rm neck})+1]\right\} - \frac{3c}{\pi}\left\{\frac{a_4}{3}\sin\left(\frac{3\pi u_{\rm neck}}{2}\right) - \frac{a_5}{4}[\cos(2\pi u_{\rm neck})-1]\right\}, \tag{A21}$$

with

$$u_{\rm neck} = \frac{4}{\pi}\frac{a_3}{a_2+9a_4}. \tag{A22}$$

That leads to

$$\alpha = \frac{3ca_3}{\pi}\left\{1 - \frac{2(a_2+a_4)}{(a_2+9a_4)}\right\}. \tag{A23}$$

The masses of the left and right nascent fragments can then be easily evaluated for any value of the mass-asymmetry α according to

$$A_L = \frac{1-\alpha}{2}A \quad \text{and} \quad A_R = A - A_L = \frac{1+\alpha}{2}A. \tag{A24}$$

6. Multipole moments

In what follows, we propose expressions for the multipole moments,

$$Q_{n0} = \iiint P_n(\cos\theta)\, r^2\, d^3r, \tag{A25}$$

where P_n are the Legendre polynomials.

For the quadrupole moment Q_{20} one obtains

$$\begin{aligned} Q_{20} &= \iiint P_2(\cos\theta)\, r^2\, d^3r \\ &= \frac{1}{2}\iiint [3\cos^2\theta - 1\,] r^2\, d^3r \\ &= \frac{1}{2}\iiint [2z^2-\rho^2]\rho\, d\rho\, d\varphi\, dz \\ &= \frac{\pi}{4}\left[4\int \rho_s^2(z)\, z^2\, dz - \int \rho_s^4(z)\, dz\right], \end{aligned} \tag{A26}$$

which yields

$$\begin{aligned} Q_{20} &= \sqrt{5\pi}\,\frac{c\,R_0^3}{2}\sum_n \left\{a_{2n}\left[z_{sh}^2\, I_{c0}^{(n)} + z_0^2\, I_{c2}^{(n)}\right]\right\} \\ &\quad + \sqrt{5\pi}\,\frac{c\,R_0^3}{2}\sum_n \left\{2\,a_{2n+1}\, z_0\, z_{sh}\, I_{s1}^{(n)}\right\} \\ &\quad - \sqrt{5\pi}\,\frac{c\,R_0^3}{2}\sum_n \left\{\frac{R_0^2}{4}\left[a_{2n}^2 + a_{2n+1}^2\right]\right\}. \end{aligned} \tag{A27}$$

The trigonometrical integrals I are written in Appendix 8. In a similar way one determines the higher order multipole moments.

7. Moments of inertia

The rigid-body moments of inertia, $\mathcal{J}_z$ for rotation around the symmetry axis, and $\mathcal{J}_y$ for rotation around an axis perpendicular to the symmetry axis, will also be calculated, where

$$\begin{aligned} \mathcal{J}_z &= \mu\iiint r_\perp^2\, d^3r = \mu\iiint \rho^2\, d^3r \\ &= \frac{\mu\,\pi}{2}\int_{z_{\rm min}}^{z_{\rm max}} \rho_s^4(z)\, dz, \end{aligned} \tag{A28}$$

and, for instance,

$$\begin{aligned} \mathcal{J}_y &= \mu\iiint (x^2+z^2)\, d^3r \\ &= \mu\iiint [\rho^2\, \cos^2\varphi + z^2]\, d^3r, \end{aligned} \tag{A29}$$

which is identical to $\mathcal{J}_x$, where μ is the mass per unit volume. For the calculation of the moments of inertia $\mathcal{J}_z$ and $\mathcal{J}_y$, one has

$$\mathcal{J}_z = \frac{\mu\pi}{2}\, c\, R_0^5 \sum_n \left[a_{2n}^2 + a_{2n+1}^2\right], \tag{A30}$$

and

$$\begin{aligned} \mathcal{J}_y &= \frac{\mu\pi}{4}\, c\, R_0^3 \sum_n \left\{R_0^2\left(a_{2n}^2 + a_{2n+1}^2\right)\right\} \\ &\quad + \frac{\mu\pi}{4}\, c\, R_0^3 \sum_n \left\{4a_{2n}\left[z_{sh}^2\, I_{c0}^{(n)} + z_0^2\, I_{c2}^{(n)}\right]\right\} \\ &\quad + \frac{\mu\pi}{4}\, c\, R_0^3 \sum_n \left\{8\, a_{2n+1}\, z_0\, z_{sh}\, I_{s1}^{(n)}\right\}. \end{aligned} \tag{A31}$$

The different trigonometric integrals I that appear in the above moments can be evaluated numerically.

8. Some auxiliary Fourier integrals

For evaluating the quadrupole moment Q_{20} in Eq. (A27) as well as the moments of inertia in Eq. (A31) the following integrals are needed:

$$\begin{aligned} I_{c0}^{(n)} &= \int_{-1}^{1} \cos\left(\frac{2n-1}{2}\,\pi\, x\right) dx = \frac{4}{(2n-1)\,\pi}\,(-1)^{n-1}, \\ I_{c2}^{(n)} &= \int_{-1}^{1} x^2\, \cos\left(\frac{2n-1}{2}\,\pi\, x\right) dx \\ &= \left[1 - \frac{2}{\pi^2}\left(\frac{2}{2n-1}\right)^2\right] I_{c0}^{(n)}, \end{aligned}$$

and

$$I_{s1}^{(n)} = \int_{-1}^{1} x\, \sin\left(\frac{2n}{2}\,\pi\, x\right) dx = \frac{2}{n\,\pi}\,(-1)^{n-1}.$$

[1] H. J. Krappe and K. Pomorski, *Theory of Nuclear Fission*, Lecture Notes in Physics 838 (Springer-Verlag, Berlin, 2012).
[2] K. Pomorski, B. Nerlo-Pomorska, J. Bartel, and C. Schmitt, Acta Phys. Pol. B **8**, 667 (2015).
[3] P. Moller, D. G. Madland, A. J. Sierk, and A. Iwamoto, Nature (London) **409**, 785 (2001).
[4] J. Bartel, K. Pomorski, and B. Nerlo-Pomorska, Acta Phys. Pol. B Sup. **10**, 17 (2017).
[5] B. Nerlo-Pomorska, K. Pomorski, J. Bartel, and C. Schmitt, Acta Phys. Pol. B (to be published) (2017).
[6] B. Nerlo-Pomorska, K. Pomorski, J. Bartel, and C. Schmitt, Acta Phys. Pol. B Sup. **10**, 173 (2017).
[7] R. W. Hasse and W. D. Myers, *Geometrical Relationships of Macroscopic Nuclear Physics* (Spinger-Verlag, Berlin, 1988).
[8] J. Bartel, F. Ivanyuk, and K. Pomorski, Int. J. Mod. Phys. E **19**, 601 (2010).
[9] M. Brack, J. Damgaard, and A. S. Jensen, Rev. Mod. Phys. **44**, 320 (1972).
[10] J. R. Nix, Nucl. Phys. A **130**, 241 (1969).
[11] P. Moller and J. R. Nix, Nucl. Phys. A **229**, 269 (1974).
[12] P. Moller (private communication).
[13] F. A. Ivanyuk and K. Pomorski, Phys. Rev. C **79**, 054327 (2009).
[14] K. Pomorski and J. Dudek, Phys. Rev. C **67**, 044316 (2003).
[15] P. Moller, J. R. Nix, W. D. Myers, and W. J. Swiatecki, At. Data Nucl. Data Tables **59**, 185 (1995).
[16] S. G. Nilsson *et al.*, Nucl. Phys. A **131**, 1 (1969).
[17] B. Nerlo-Pomorska, K. Pomorski, and C. Schmitt, Phys. Scr. **154**, 014026 (2013).
[18] V. M. Strutinsky, Nucl. Phys. A **95**, 420 (1967).
[19] P. Moller, Nucl. Phys. A **192**, 529 (1972).
[20] A. Dobrowolski, K. Pomorski, and J. Bartel, Comput. Phys. Commun. **199**, 118 (2016).
[21] K. T. R. Davies and J. R. Nix, Phys. Rev. C **14**, 1977 (1976).
[22] A. Gozdz and K. Pomorski, Nucl. Phys. A **451**, 1 (1986).
[23] B. Nerlo-Pomorska, K. Pomorski, C. Schmitt, and J. Bartel, Phys. Scr. **89**, 054031 (2014).
[24] B. Nerlo-Pomorska, K. Pomorski, C. Schmitt, and J. Bartel, Phys. Scr. **90**, 114010 (2015).
[25] I. V. Ryzhov *et al.*, Phys. Rev. C **83**, 054603 (2011).
[26] K. Pomorski, Phys. Rev. C **70**, 044306 (2004).
[27] K. Pomorski and F. Ivanyuk, Int. J. Mod. Phys. E **18**, 900 (2009).
[28] K. Pomorski, Comput. Phys. Commun. **174**, 181 (2006).
[29] B. N. Lu, E. G. Zhao, and S. G. Zhou, Phys. Rev. C **85**, 011301(R) (2012).
[30] A. Dobrowolski, K. Pomorski, and J. Bartel, Phys. Rev. C **75**, 024613 (2007).
[31] B. Nerlo-Pomorska, K. Pomorski, J. Bartel, and C. Schmitt, Eur. Phys. J. A (to be published) (2017).
[32] A. Bohr, Kgl. Danske Vid. Selsk. Mat. Fys. Medd. **26**, 14 (1952).
[33] P. Jachimowicz, M. Kowal, and J. Skalski, Phys. Rev. C **85**, 034305 (2012).
[34] K.-H. Schmidt *et al.*, Nucl. Phys. A **665**, 221 (2000).
[35] A. N. Andreyev *et al.*, Phys. Rev. Lett. **105**, 252502 (2010).
[36] T. Ichikawa, A. Iwamoto, P. Moller, and A. J. Sierk, Phys. Rev. C **86**, 024610 (2012).
[37] A. V. Andreev, G. G. Adamian, N. V. Antonenko, and A. N. Andreyev, Phys. Rev. C **88**, 047604 (2013).
[38] S. Panebianco, J. L. Sida, H. Goutte, J. F. Lemaitre, N. Dubray, and S. Hilaire, Phys. Rev. C **86**, 064601 (2012).
[39] J. D. McDonnell, W. Nazarewicz, J. A. Sheikh, A. Staszczak, and M. Warda, Phys. Rev. C **90**, 021302 (2014).
[40] L. Ghys *et al.*, Phys. Rev. C **90**, 041301 (2013).
[41] E. Prasad *et al.*, Phys. Rev. C **91**, 064605 (2015).
[42] K. Ramachandran *et al.*, EPJ Web of Conf. **63**, 02017 (2013).
[43] K. Nishio *et al.*, Seminar at the INT 13-3 Workshop, Seattle (2013).
[44] K. Nishio *et al.*, Phys. Lett. B **748**, 89 (2015).
[45] A. Chatillon *et al.*, Studies On Fission with Aladin, NUFRA2013, Kemer, Turkey (2013).
[46] V. L. Truesdale *et al.*, Phys. Rev. C **94**, 034308 (2016).
[47] J. Weber *et al.*, Phys. Rev. C **13**, 2413 (1976).
[48] J. Randrup and P. Moller, Phys. Rev. Lett. **106**, 132503 (2011).
[49] Y. Aritomo, S. Chiba, and F. Ivanyuk, Phys. Rev. C **90**, 054609 (2014).
[50] M. G. ltkis *et al.*, Yad. Fiz. **53**, 1225 (1991) [Sov. J. Nucl. Phys. **53**, 757 (1991)].
[51] L. Dematte *et al.*, Nucl. Phys. A **617**, 331 (1997).
[52] K. Pomorski, B. Nerlo-Pomorska, J. Bartel, and C. Schmitt, Acta Phys. Pol. B Supl. **10**, 183 (2017).
[53] P. A. Butler and W. Nazarewicz, Rev. Mod. Phys. **68**, 349 (1996).
[54] S. E. Agbemava, A. V. Afanasjev, and P. Ring, Phys. Rev. C **93**, 044304 (2016), and references therein.
[55] B. Nerlo-Pomorska, K. Pomorski, and J. Bartel, Acta Phys. Pol. B **47**, 1001 (2016).
[56] M. Kowal and J. Skalski, Phys. Rev. C **85**, 061302 (2012).
[57] T. Ichikawa, P. Moller, and A. J. Sierk, Phys. Rev. C **87**, 054326 (2013).
[58] J. D. McDonnell, W. Nazarewicz, and J. A. Sheikh, Phys. Rev. C **87**, 054327 (2013).
[59] L. Csige *et al.*, Phys. Rev. C **85**, 054306 (2012).
[60] J. Sadhukhan, W. Nazarewicz, and N. Schunck, Phys. Rev. C **93**, 011304 (2016).
[61] K. Pomorski *et al.*, Nucl. Phys. A **679**, 25 (2000).